FULL PAPER

Chalcogenide Nanopillars

NANO · MICRO
small
www.small-journal.com

Check for updates

High-Density Sb$_2$Te$_3$ Nanopillars Arrays by Templated, Bottom-Up MOCVD Growth

Raimondo Cecchini,* Raja S. R. Gajjela, Christian Martella, Claudia Wiemer, Alessio Lamperti, Lucia Nasi, Laura Lazzarini, Luca G. Nobili, and Massimo Longo*

Sb$_2$Te$_3$ exhibits several technologically relevant properties, such as high thermoelectric efficiency, topological insulator character, and phase change memory behavior. Improved performances are observed and novel effects are predicted for this and other chalcogenide alloys when synthetized in the form of high-aspect-ratio nanostructures. The ability to grow chalcogenide nanowires and nanopillars (NPs) with high crystal quality in a controlled fashion, in terms of their size and position, can boost the realization of novel thermoelectric, spintronic, and memory devices. Here, it is shown that highly dense arrays of ultrascaled Sb$_2$Te$_3$ NPs can be grown by metal organic chemical vapor deposition (MOCVD) on patterned substrates. In particular, crystalline Sb$_2$Te$_3$ NPs with a diameter of 20 nm and a height of 200 nm are obtained in Au-functionalized, anodized aluminum oxide (AAO) templates with a pore density of ≈5 × 10^{10} cm^{-2}. Also, MOCVD growth of Sb$_2$Te$_3$ can be followed either by mechanical polishing and chemical etching to produce Sb$_2$Te$_3$ NPs arrays with planar surfaces or by chemical dissolution of the AAO templates to obtain freestanding Sb$_2$Te$_3$ NPs forests. The illustrated growth method can be further scaled to smaller pore sizes and employed for other MOCVD-grown chalcogenide alloys and patterned substrates.

Dr. R. Cecchini, R. S. R. Gajjela,[+] Dr. C. Martella, Dr. C. Wiemer,
Dr. A. Lamperti, Dr. M. Longo
CNR-IMM
via C. Olivetti 2, 20864 Agrate Brianza, MB, Italy
E-mail: raimondo.cecchini@mdm.imm.cnr.it;
massimo.longo@mdm.imm.cnr.it
R. S. R. Gajjela, Prof. L. G. Nobili
Dipartimento di Chimica
Materiali e Ingegneria Chimica "Giulio Natta,"
Politecnico di Milano
Via Mancinelli 7, 20131 Milano, Italy
Dr. L. Nasi, Dr. L. Lazzarini
CNR-IMEM
Parco Area delle Scienze 37/A, 43124 Parma, Italy

The ORCID identification number(s) for the author(s) of this article can be found under https://doi.org/10.1002/smll.201901743.

[+]Present address: Department of Applied Physics, Eindhoven University of Technology, 5612 AE, Netherlands

1. Introduction

Developments in the fabrication of low-dimensional chalcogenide nanostructures are a key factor for their integration into novel, high performing electrical devices. In particular, high-aspect-ratio chalcogenide nanostructures, such as nanowires (NWs) and nanopillars (NPs), are especially interesting for the realization of advanced thermoelectric, spintronic, and memory devices. Among chalcogenide alloys, Sb$_2$Te$_3$ exhibits several desirable properties, including phase change memory (PCM) behavior with high switching speed,[1,2] high Seebeck coefficient,[3–5] and topological insulator properties.[6,7] High-aspect-ratio nanostructures of Sb$_2$Te$_3$ and other chalcogenide alloys are expected to bring important advantages in all the above-mentioned applications. Indeed, the reduction of the programming power in NW-based, compared to thin film-based, PCM cells has been predicted[8] and widely demonstrated.[9–11] A higher figure of merit is expected for thermoelectric generators built on chalcogenide NWs, NPs and other nanostructures.[12–14] Further, it is anticipated that topological insulator NWs will allow innovative device concepts in spintronics.[15–17] Despite their high technological potential, the integration of low-dimensional chalcogenide nanostructures into architectures relevant for industrial applications remains challenging. In particular, a high degree of control over the position and size distribution of the NPs/NWs is required, as well as their embedment in a, e.g., electrically insulating matrix. In principle, this can be achieved by filling with the chalcogenide alloy the high-aspect-ratio trenches/pores preformed on nanopatterned substrates. However, line-of-sight deposition processes are inherently inadequate for such a task. In the fabrication of PCM devices, for example, conformal growth of chalcogenide thin films by chemical vapor deposition (CVD) and atomic layer deposition has been proposed to replace magnetron sputtering in, e.g., so-called "confined" PCM memory cells architectures.[18–20] Nevertheless, even these implementations do not take full advantage of the bottom-up growth potential available to CVD-based processes. Indeed, CVD and, in particular, metal organic chemical vapor deposition (MOCVD) processes allow the bottom-up growth of nanostructures and NWs of a wide range

ADVANCED
SCIENCE NEWS
www.advancedsciencenews.com

NANO · MICRO
small
www.small-journal.com

of chalcogenide alloys with often single-crystal quality, which is often out of the reach for other methods. On the other hand, these types of synthesis have in most cases been performed on planar, unpatterned substrates, therefore leading to a random distribution of the NWs.[21–25] The growth of ordered arrays of nanocrystals of different chalcogenide alloys, including Sb_2Te_3, by selective MOCVD growth has been demonstrated on low aspect-ratio lithographically patterned (≈100 nm size) templates and on substrates locally treated by oxygen plasma, as well as using Au nanodeposits as catalyzers exploiting the vapor–liquid–solid mechanism.[26–31] For what concerns high-aspect-ratio chalcogenide nanostructures, the growth of Te-rich Sb_2Te_3 NWs exploiting the vapor–solid mechanism on substrates patterned with pores of diameter ≈50 nm and height ≈100 nm has been explored.[32] Clearly, further downscaling of the chalcogenide NPs/NWs size and higher arrays densities should be demonstrated in order for selective bottom-up (MO)CVD methods to replace the processes presently used in the fabrication of, e.g., state-of-the-art PCM cells, and enable the realization of the next generation of thermoelectric and spintronic devices.

The alternative method to the MOCVD proposed here for the template-based filling with chalcogenide NPs or NWs arrays is electrodeposition. Few reports can be found on the obtainment of ordered and dense arrays of Sb_2Te_3 NWs through electrodeposition into nanoporous anodic aluminum oxide (AAO) templates. Sb–Te NWs with different compositions have been electrodeposited with an average diameter of 80 nm and length of 1.2 μm (aspect ratio = 15); however, they were amorphous.[33] To find similar sizes to those we considered in the present work, we need to refer to Bi_2Te_3 NWs: their electrodeposition with diameters down to around 25 nm was reported in ref. [34]. In this case, the NWs were polycrystalline and with an incomplete filling of the high aspect ratio pores. Deposition of ordered arrays of Sb–Te NWs with diameters down to 100 nm with a mixed amorphous structure, which was then transformed into a crystalline one upon annealing, was described in ref. [35]. To our knowledge, the minimum Sb_2Te_3 NPs or NWs diameter reported is of 50 nm, obtained in AAO templates with an aspect ratio ≈500 and a density that can be estimated around 1×10^{10} cm^{-2}.[36] Noteworthy, electrodeposition needs a conductive substrate and current has to be provided to the cathode, in order to obtain growth. This requirement could be difficult to be guaranteed in an industrial implementation and it would, in any case, require an ad hoc design of the system/process flow; on the contrary, MOCVD does not need such a condition. Furthermore, it has to be considered that, unlike electrodeposition, the growth of a wide range of chalcogenide alloys (including Ge–Te, Ge–Sb–Te, In–Sb–Te, In–Sb, and In–Te) in the form of NWs has been demonstrated by MOCVD, together with the assessment of their PCM behavior.[37]

In the present work, using Au-functionalized AAO templates, we show that the fabrication of arrays of crystalline Sb_2Te_3 NPs with diameters of ≈20 nm, aspect-ratio of ≈10, and surface density of ≈5×10^{10} cm^{-2} can be attained by an MOCVD bottom-up growth process. The presently illustrated approach can equally be applied to standard lithographically patterned templates. On the other hand, thanks to their small pore sizes, low cost, and self-assembly fabrication over large areas, AAO templates might represent a competitive alternative for the integration of chalcogenide high-aspect-ratio nanostructures in functional devices.[38–41] Finally, we show two possible post-MOCVD growth processes: i) "polishing-etching" (PE), consisting in the mechanical polishing and chemical etching of the top surface to remove the outgrowths, resulting in a planar surface of the NPs array and ii) liberation process (LP), where dissolution of the AAO template is performed, to obtain forests of Sb_2Te_3 NPs, freestanding on a Sb_2Te_3 film.

A schematic description of the different investigated processes is reported in **Figure 1**: Figure 1a illustrates the selective, bottom-up MOCVD growth of Sb_2Te_3 NPs in the pores of the Au-functionalized AAO templates; Figure 1b,c sketches the postgrowth processes (i) and (ii), respectively.

2. Results and Discussion

The formation of Sb_2Te_3 NPs in the pores of an AAO template with ≈20 nm average pore diameter and 200 nm height is shown in the scanning electron microscope (SEM) images reported in **Figure 2**. As it can be seen, the MOCVD growth led to the formation of the Sb_2Te_3 NPs, which first filled in the pores and then extended outside them into "outgrowths," which either maintained an NP-like shape or formed 3D crystals (Figure 2a).

For optimized MOCVD parameters (see the Experimental Section), the growth of the Sb_2Te_3 NPs turned out to be extremely selective: it is promoted by the presence of the Au deposits at the pores bottom and, in the absence of Au deposit, no growth is observed. When the Au deposit is present in the pores, the filling ratio (the ratio of the number of filled pores over the number of pores present) is about 90%, as can be seen in Figure 2b, which shows a template where partial etching of the Al_2O_3 was performed by immersion of the sample in 5 M NaOH for 15 s to expose the NPs tips (see also Supporting Information, Evaluation of filling ratio).

As from the above-mentioned postgrowth process i) PE, we investigated mechanical polishing and selective chemical etching to obtain a flat top surface without outgrowths over large areas. In Figure 2c,d, the SEM images of an AAO template after the MOCVD growth of Sb_2Te_3, followed by the mechanical polishing and chemical etching of the sample top surface described in the Experimental Section and in Figure 1b, are reported. This procedure resulted in a planar and clean top surface.

The growth of NPs inside AAO templates with pores with average diameters of ≈10 nm and heights of 150 nm was also explored (**Figure 3**). The ratio of filled pores, in this case, resulted to be much lower than for AAO templates with larger pore diameters (20 and 30 nm). Indeed, these AAO templates had a relatively broad distribution of pores diameters and irregularly shaped (e.g., branched) pores profiles. SEM analysis on templates cross-sections, before and after growth, seems to indicate that the main factor limiting the NPs formation was the presence of branched pores: on the one hand the irregular pores profile might hamper the progress of the NPs growth; on the other hand, it might prevent the formation of an Au deposit during electrodeposition on the pores bottom, which is necessary to catalyze the initial stages of the NPs formation. Nevertheless, SEM observations showed the presence of growth inside some pores as small as 10 nm. These results indicate the feasibility of downscaling the proposed MOCVD growth process to such pore sizes.
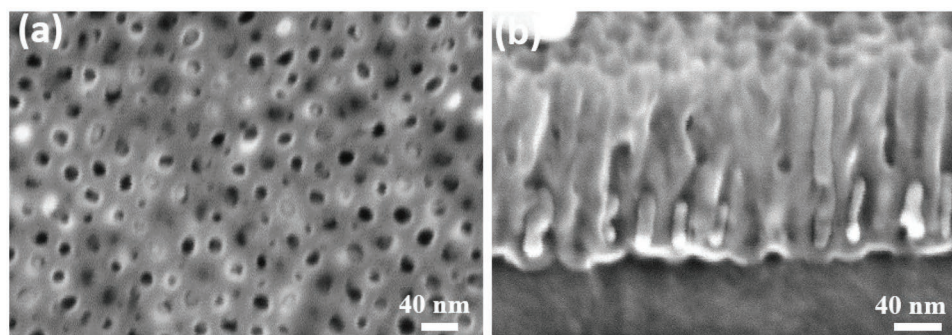
ADVANCED
SCIENCE NEWS
www.advancedsciencenews.com

NANO · MICRO
small
www.small-journal.com
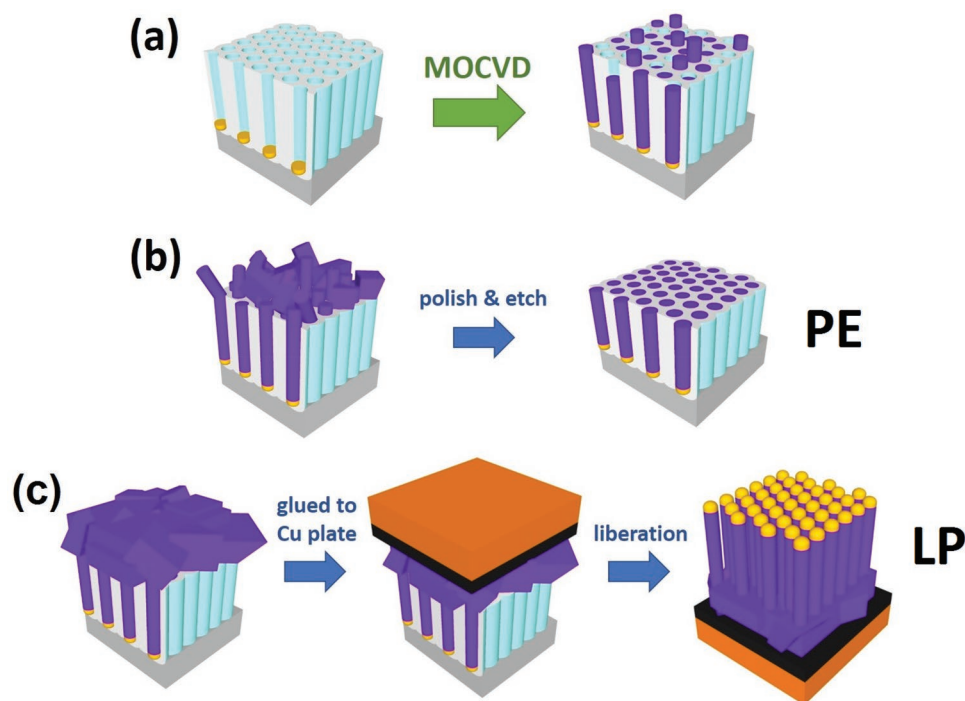
Figure 1. A schematic description of a) selective bottom-up MOCVD growth of Sb_2Te_3 NPs in the pores of Au-functionalized AAO templates. In (b) and (c) the description of two postgrowth processes: i) PE b) outgrowths are removed by a mechanical and chemical process to obtain a planar surface; or ii) LP c) a continuous Sb_2Te_3 film is formed on top of the NPs, the sample is then glued by carbon adhesive (black layer) to a copper plate (orange layer) and, finally, the AAO template is dissolved to obtain Sb_2Te_3 NPs forests standing on the Sb_2Te_3 film.
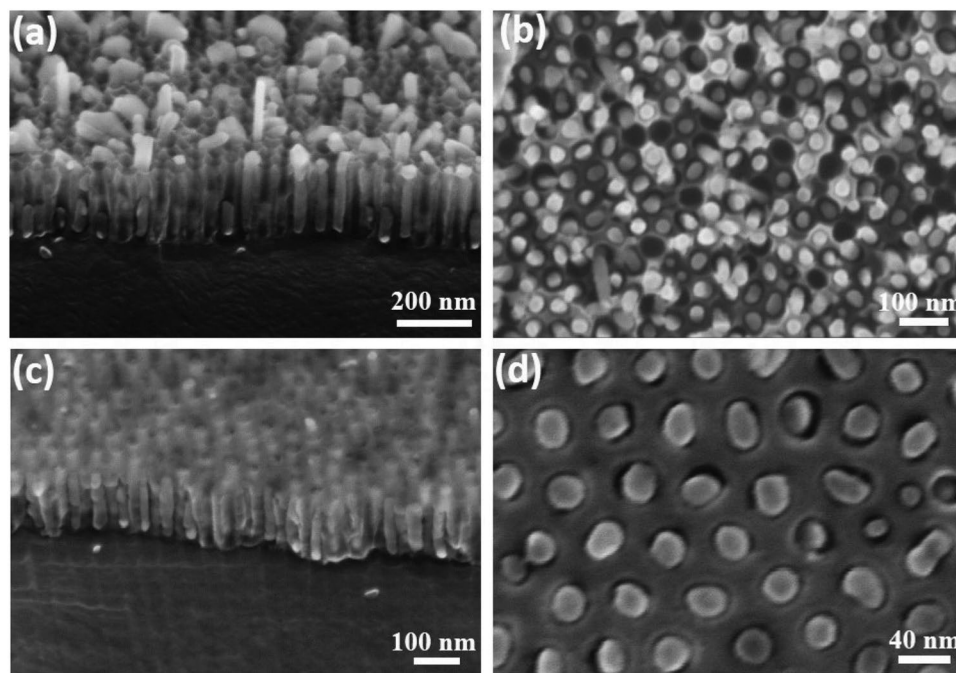
Figure 2. a) Tilted view SEM images of a cross-section of an AAO template with ≈20 nm average pore width and 200 nm pore height, after the MOCVD growth of Sb_2Te_3 ($P_R = 50$ mbar, $T_R = 300$ °C, $P_{Sb} = 9.1 \times 10^{-4}$ mbar, $P_{Te} = 1.32 \times 10^{-3}$ mbar, deposition time = 120 min). b) Plan-view SEM image of an AAO template after MOCVD growth of Sb_2Te_3 ($P_R = 25$ mbar, $T_R = 350$ °C, $P_{Sb} = 1.51 \times 10^{-3}$ mbar, $P_{Te} = 2.20 \times 10^{-3}$ mbar, deposition time = 60 min), followed by partial etching of the Al_2O_3 pores, showing the Sb_2Te_3 NPs tips exposed. c) Tilted view of a cross-section and d) plan-view of the surface of an AAO template after Sb_2Te_3 NPs growth ($P_R = 25$ mbar, $T_R = 350$ °C, $P_{Sb} = 3.02 \times 10^{-3}$ mbar, $P_{Te} = 4.40 \times 10^{-3}$ mbar, deposition time = 30 min), followed by process i) PE.

1901743 (3 of 9)

ADVANCED
SCIENCE NEWS
www.advancedsciencenews.com

NANO · MICRO
small
www.small-journal.com

Figure 3. a) SEM plan-view image of an AAO template with average pores diameter of ≈10 nm and height of 150 nm, after Sb_2Te_3 growth and planarization (postgrowth process i) PE). b) SEM tilted view image of an AAO cross-section after the MOCVD growth. In (a) it can be seen that some of the pores (including pores with diameter ≈10 nm) are filled. The limited filling density visible in (a) is likely due to the irregular shape of the pores profile, as shown in (b), and to the absence of Au in some pores.

The microstructure and composition of the NPs grown inside the AAO pores were investigated by transmission electron microscopy (TEM) and energy dispersive X-ray microanalysis (EDX). TEM and TEM-EDX analyses were performed on cross-section lamellae prepared by focused ion beam (FIB) from an AAO template with pores diameter of 20 nm and height of 180 nm, after MOCVD growth, mechanical polishing, and chemical etching of the top surface (**Figures 4** and **5**).

This analysis confirmed the filling of the pores during the Au-catalyzed MOCVD growth process and the resulting formation of NPs (Figure 4; in this figure and in Figure 5, the height of the NPs is about 110 nm, smaller than the as-grown one, due to the postgrowth process i) PE). The determination of the crystallographic properties of the NPs by high-resolution (HR)-TEM was particularly difficult, mainly due to the amorphization damage induced by the FIB preparation and the limited possibility of tilting the specimen. However, for several NPs it was possible to evidence their crystalline quality. In these cases, the NPs resulted to be single crystalline (sometimes slightly defected), as for the NP shown in Figure 4c, where the direct observation of lattice fringes along the NP length can be appreciated. The line pattern they form is due to the presence of the so-called van der Waals gaps that separate, perpendicularly to the *c*-axis, each of the three building blocks forming the unit cell of Sb_2Te_3.[43] This layered structure, typical also of Bi_2Te_3, Bi_2Se_3, and other chalcogenide alloys, including transition metal dichalcogenides,[44] is related to several of the properties
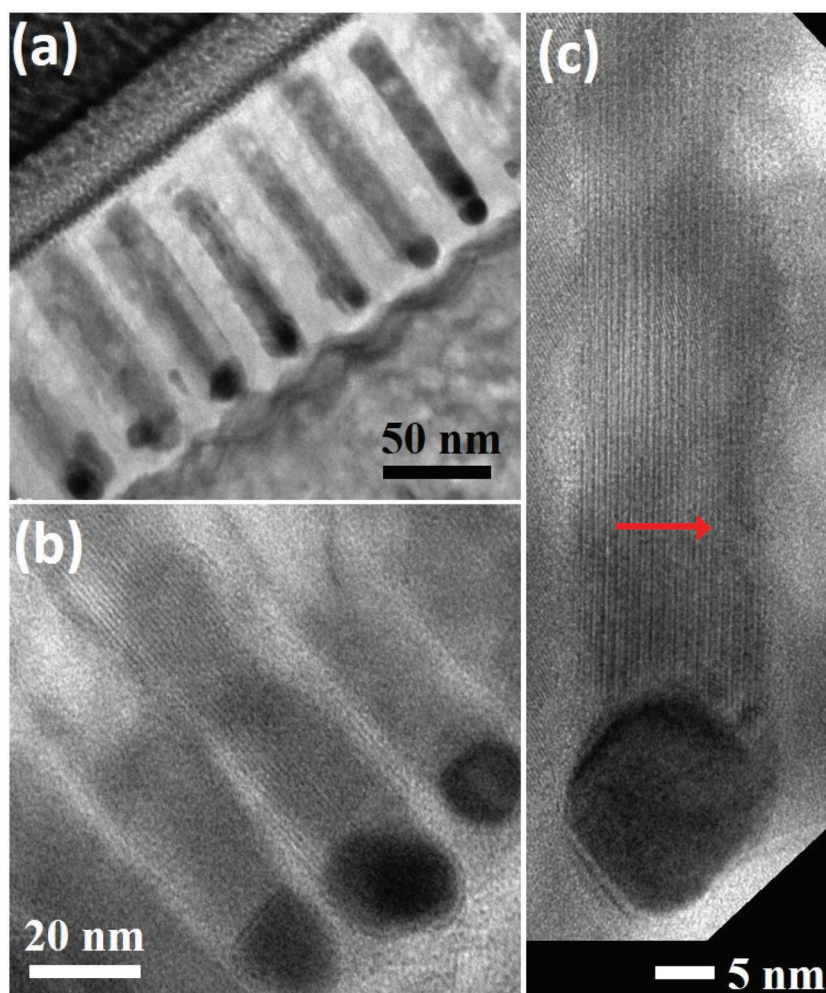
Figure 4. a) TEM image of a cross-section lamella prepared by FIB from an AAO template after MOCVD growth of Sb_2Te_3 NPs, followed by postgrowth process i) PE. HR-TEM image of b) three NPs and c) one single-crystalline NP; the *c*-axis (red arrow) of the corresponding rhombohedral Sb_2Te_3 phase is in this case orthogonal to the growth direction of the NP, similarly to what observed in MOCVD grown NWs of the Ge–Sb–Te family.[22,42]
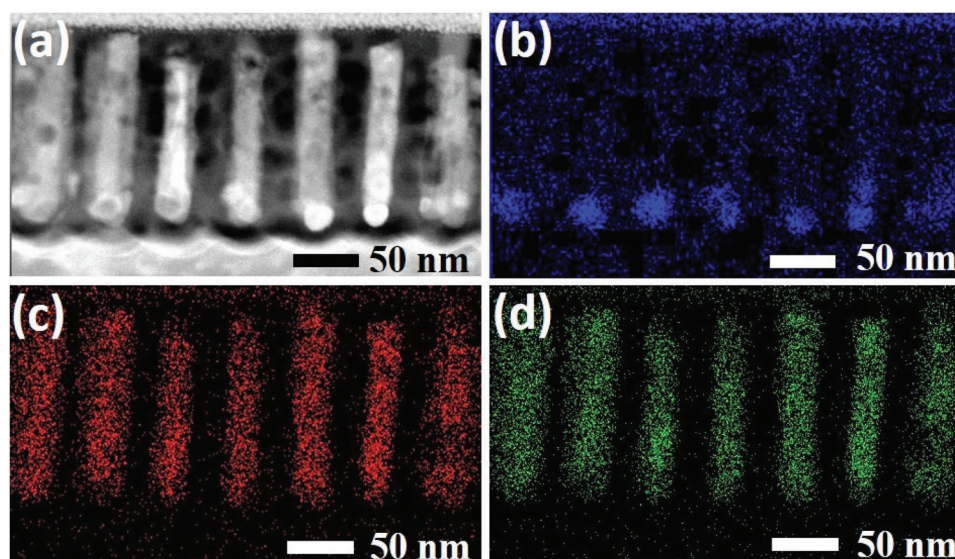
Figure 5. a) Typical Scanning-TEM (STEM) image of an AAO cross-section after NPs growth and postgrowth process i) PE; corresponding distribution maps of b) Au, c) Sb, and d) Te respectively, obtained with the X-ray L lines of each element measured by EDX.

that make these materials interesting for application. It is for instance linked to the anisotropic behavior of the electronic and thermal transport properties of this class of materials[45,46] and thought to be related to the presence of their topological properties[47] as well as in the nonvolatile memory switch mechanism.[48] Hence the importance of developing technologically suitable processes to fabricate highly textured Sb_2Te_3, alternative to molecular beam epitaxy (MBE) grown films. A possible approach aims at growing high-quality crystals of limited extension but on predetermined positions. (MO)CVD growth of single-crystals platelets with partially controlled dimensions and orientation in arrays was reported in refs. [26–31]. Here it is shown that the same level of crystal quality is reproduced on a pillar, rather than platelets geometry, and in a density that exceeds by orders of magnitude those reported in the above-mentioned references. Moreover, as shown above, in many NPs where the tilting around the NP axis is favorable, HR-TEM indicated a preferential orientation of the van der Waals gaps parallel to the NP length. This arrangement is perpendicular to the one obtained in films deposited by MBE, as well as to the one commonly observed in horizontally lying, MOCVD grown platelets, and could be important in the case of a vertical device geometry. Crystalline, and hence electrically conductive state, of the as-grown NPs was assessed also by conductive-atomic force microscopy (c-AFM). Despite the presence of the aluminum oxide barrier layer at the bottom of the pores, clear electrical contrast ascribed to the NPs was evidenced (see Supporting Information, C-AFM measurements).

The analysis of the diffraction patterns taken on many liberated NPs (see Supporting Information, Supplementary TEM analyses) indicated that the crystallographic structure of the NPs corresponds to the rhombohedral phase of Sb_2Te_3.

The NPs exhibited also a uniform composition, as proved by the related TEM-EDX analysis (Figure 5). The fit of the EDX spectra taken in several regions of the lamella (see Supporting Information, Supplementary TEM analyses) gave a composition of Sb = 0.31 and Te = 0.69 (in at%), corresponding to an excess of Te with respect to the stoichiometric Sb_2Te_3 composition. No Au was detected by EDX in the NPs.

The microstructure of the Sb_2Te_3 NPs was also analyzed by X-ray diffraction (XRD) and Raman spectroscopy measurements, both on the as-grown and PE (i.e., after the postgrowth process (i)) samples, in order to take into account the contribution given by the NPs and the outgrowths, which are removed by the PE process. Consistently with TEM diffraction, the XRD pattern of an as-grown sample, reported in **Figure 6**a, indicates the presence of the polycrystalline rhombohedral phase of Sb_2Te_3[49] (peaks relative to the aluminum substrate are also present; see Supporting Information, Supplementary XRD analyses). As expected, the intensities of all the peaks relative to the Sb_2Te_3 phase are very much reduced after the chemical and mechanical cleaning of the sample surface. Also, due to the overlapping of some of the Sb_2Te_3 and Al diffraction peaks, it was difficult to derive an indication on the preferential orientation of the NPs.

The Raman spectra of an as-grown and of a mechanically chemically cleaned sample are reported in Figure 6b. On the as-grown sample, the Raman peaks are visible at ≈120, ≈140, and ≈167 cm^{-1}, while, after the removal of the outgrowths, peaks are present at ≈113, ≈125, ≈140, and ≈167 cm^{-1}. The peaks at ≈113 and ≈167 cm^{-1} can be attributed to, respectively, the E^2_g and A^2_{1g} modes of Sb_2Te_3.[50–52] The Raman peak at ≈140 cm^{-1}, visible both before and after cleaning, can be attributed to the E^2 modes of pure Te–Te bonds.[53] Also the peak at ≈125 cm^{-1}, visible after cleaning, has been related to pure Te bonds, namely to the A^1 modes.[53] The presence of pure Te bonds could be related to Te precipitation, due to an excess of this element with respect to the stable Sb_2Te_3 stoichiometric composition, as observed in thermally evaporated Sb_2Te_3 films[54] and in Sb_2Te_3 NWs grown by a vapor–solid method in nanosized templates.[32] Surface precipitation of Te has also been observed by Raman spectroscopy in Sb_2Te_3 deposited by physical vapor transport.[51] Finally, in mechanically alloyed Sb_2Te_3, the presence of Te–Te
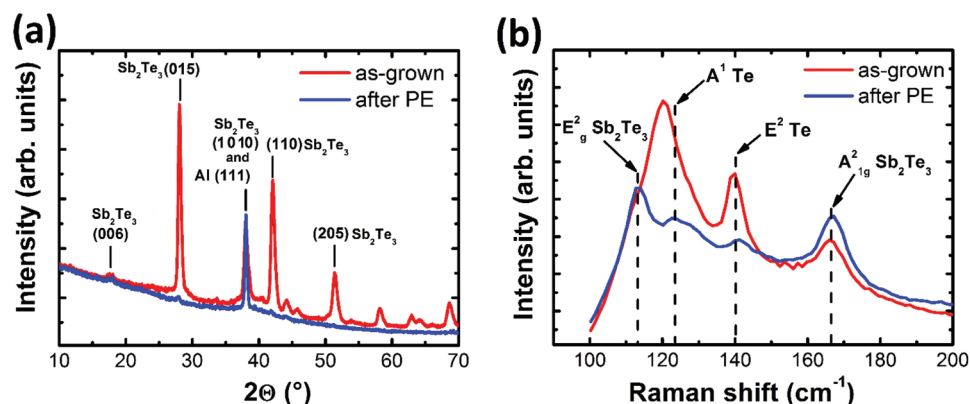
Figure 6. a) XRD and b) Raman measurements performed on an AAO template after NPs growth: before (red curve) and after (blue curve) the post-growth cleaning PE process i) to remove the outgrowths. The positions of the main XRD peaks of Sb_2Te_3 and of Al are indicated in (a) and the position of the Raman peaks of Sb_2Te_3 and of Te–Te bonds are indicated in (b).

bonds has been detected by Raman spectroscopy and attributed to Te particles, while the concomitant absence of Te peaks in the XRD pattern has been explained with a limited amount of Te phase.[55] As noted before, an excess of Te with respect to the Sb_2Te_3 stoichiometry in the presently studied NPs was evidenced by TEM-EDX. Interestingly, the relative intensity of the Sb_2Te_3 related peaks ($\approx$113 and $\approx$167 cm^{-1}) increased with respect to the Te–Te peak ($\approx$140 cm^{-1}) after cleaning. Further, the peak present at $\approx$120 cm^{-1} before cleaning shows a shoulder at lower shift values, indicating the contribution of an additional mode. The peak at $\approx$120 cm^{-1} could, in fact, be due to the superposition of the $\approx$113 cm^{-1} E^2_g mode of Sb_2Te_3 and the $\approx$125 cm^{-1} A^1 mode of Te, which, after the cleaning, appears in place of the peak at $\approx$120 cm^{-1}. This change could indicate that the presence of the pure Te phase is higher in the outgrowths, with respect to the NPs: the removal of most of the pure Te phase, together with the outgrowths during cleaning, decreases the contribution of the A^1 mode of Te, so that both peaks, the E^2_g of Sb_2Te_3 and A^1 of Te, are resolved in the Raman spectra of cleaned samples. The sharpness of the Sb_2Te_3 peaks measured on the cleaned samples is comparable to that observed in refs. [50] and [52] for crystalline Sb_2Te_3 (in particular the full widths at half maximum of the Sb_2Te_3 Raman peaks at $\approx$113 and $\approx$167 cm^{-1}, equal to $\approx$10 and $\approx$12 cm^{-1}, respectively, are very close to the value reported in refs. [51] and [54]).
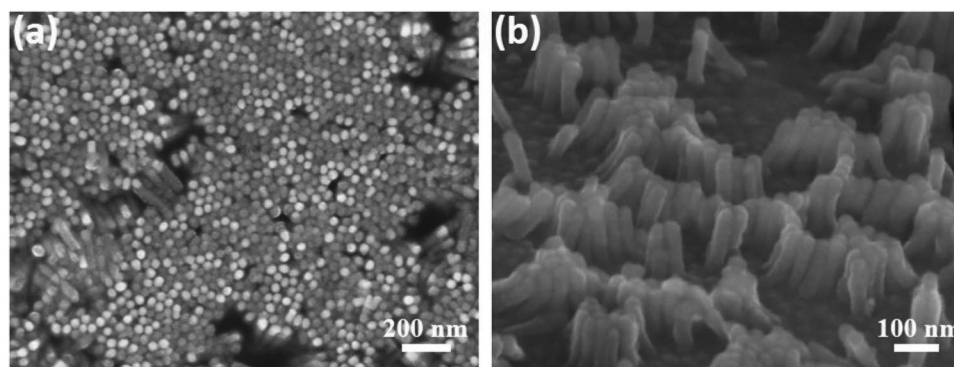
The morphological and microstructural analyses illustrated so far allow to draw some general considerations on the growth mechanism of the NPs. As seen by SEM and TEM investigations, the growth of the Sb_2Te_3 NPs is clearly bottom-up and highly selective on the Au-functionalized pores. TEM-EDX investigated areas show that Au is still present at the pores bottom after the growth (Figure 5d). This finding points to a growth mechanism different from the vapor–liquid–solid or vapor–solid–solid mechanisms, which are often encountered in the MOCVD growth of metal nanoparticles-catalyzed NWs.[56–60] In these types of growth, the NWs/NPs form below the catalyst metal particle, which is lifted by the growing NW/NPs and should be therefore present only on their tip. On the other hand, the surface selective CVD growth of different metals and chalcogenides films and NWs by vapor–solid processes is well documented.[61–63] For instance, the fabrication of arrays of

Sb_2Te_3, Bi_2Te_3, and $SnSe_2$ crystals grown on TiN exposed in a SiO_2 matrix has been demonstrated.[26–28,30] Similarly, the role of Au in our case could consist in catalyzing the initial steps of the NPs growth, e.g., by favoring the Sb and Te precursors dissociation and the nucleation of the Sb_2Te_3 phase, with subsequent preferential growth occurring on the already formed Sb_2Te_3 deposit.

Finally, we show that the AAO templates can also be used to fabricate dense forests of Sb_2Te_3 NPs, following the postgrowth process ii) LP, illustrated in Figure 1c. As noted before, when reaching the pores top, the growing NPs tend to form larger crystals. Prolonging the MOCVD for long times resulted in the coalescence of these outgrowths and eventually in the formation of a relatively uniform Sb_2Te_3 film on top of the AAO. The morphology (see Supporting Information, Sb_2Te_3 NPs forests) of this film is similar to that reported for MOCVD grown polycrystalline Sb_2Te_3 films.[64] As from the sketch of Figure 1c, the Sb_2Te_3 film was glued to a copper substrate and the template was dissolved by immersion in the 3.75 M NaOH solution. SEM images of a sample at the end of this process sequence are reported in **Figure 7**. An AAO template with 30 nm average pore width and 150 nm pore height was used in this case. The resulting structure consisted of highly dense Sb_2Te_3 NPs forests (Figure 7a) standing on the Sb_2Te_3 film (Figure 7b). The Sb_2Te_3 NPs had the expected morphology, i.e., they replicated the pores of the used AAO template (Figure 7b; see also Supporting Information, Sb_2Te_3 NPs forests, for additional SEM images of NPs forests on Sb_2Te_3 films).

3. Conclusions

We demonstrated the use of MOCVD for the fabrication of Sb_2Te_3 nanopillars, inside high-aspect-ratio, highly scaled and dense templates. In particular, we filled by a crystalline Te-rich Sb_2Te_3 alloy the pores of AAO templates with pore diameters down to 20 nm, height up to 200 nm and density $\approx$5 × 10^{10} cm^{-2}, obtaining filling ratios $\approx$90%. The feasibility of growth inside pores of $\approx$10 nm width was also proved. These results show the potentiality of bottom-up MOCVD-based processes for the integration of ultrascaled, high-aspect-ratio chalcogenide

**ADVANCED
SCIENCE NEWS**

www.advancedsciencenews.com

**NANO · MICRO
small**

www.small-journal.com

Figure 7. SEM a) plan-view image of a forest of Sb_2Te_3 NPs standing on a Sb_2Te_3 film, after the postgrowth process ii) LP, sketched in Figure 1c (MOCVD growth process parameters: P_R = 25 mbar, T_R = 350 °C, P_{Sb} = 3.0×10^{-3} mbar, P_{Te} = 4.4×10^{-3} mbar, deposition time = 240 min); b) tilted view of the NPs in a region with lower density. The lower density of NPs in the region shown in (b) compared to (a) is due to truncation of the NPs during template detachment (the base of the truncated NPs is still visible). The morphology of the NPs replicates the type of AAO template used (i.e., ≈30 nm pore width and 150 nm height).

nanostructures in high-density arrays for advanced phase change memory, thermoelectric generators, and topological insulator-based devices. Finally, the described combination of self-assembled AAO templates and MOCVD can be effectively used to fabricate innovative structures over large areas and at a relatively low cost. Also, this approach could be replicated on other substrates, including Si, onto which the fabrication of AAO templates has already been proved.[58,65–67]

4. Experimental Section

Au-Functionalized AAO Templates: The templates were AAO membranes,[68,69] with electrodeposited Au at the pores bottom commercially available at InRedox (USA). AAO templates with pore diameters of, respectively, ≈10, 20, and 30 nm and height in the range of (120–200) nm were used, while the volume of the Au deposit was in the range of (5–50) $\times 10^3$ nm^3 (see Supporting Information, Fabrication of AAO templates).

MOCVD Growth: The growth of Sb_2Te_3 was performed in an Aixtron AIX 200/4 MOCVD reactor. The precursors were electronic grade antimony trichloride ($SbCl_3$) and bis(trimethylsilyl)telluride ($Te(SiMe_3)_2$), provided by Air Liquide, and transported to the MOCVD reactor by ultrapurified N_2 gas.[70] The partial pressures in the vapor phase of $SbCl_3$ (P_{Sb}) and $Te(SiMe_3)_2$ (P_{Te}) were varied in the range of (4.5×10^{-4}–1.1×10^{-2}) and (6.6×10^{-4}–1.6×10^{-2}) mbar, respectively, with a fixed ratio P_{Sb}: P_{Te} = 1: 1.46. The reactor temperature (T_R) and reactor pressure (P_R) were varied in the range of (80–400) °C and (15–300) mbar, respectively. The deposition times ranged from 15 to 240 min.

Highly selective growth in the pores was observed for T_R between 250 and 350 °C. At lower temperatures, the selectivity was reduced and at T_R = 80 °C a continuous Sb_2Te_3 film formed on top of the AAO surface. For T_R above 350 °C, the amount of grown material decreased and almost no growth was observed for T_R = 400 °C. Within the (250–350) °C temperature range, no significant effect of P_R was observed. The increase of the reactants partial pressures, with a fixed ratio of P_{Sb}: P_{Te} = 1: 1.46, did not affect the growth, except for what concerns the growth rate, which was higher for higher reactant partial pressures.

Postgrowth Processes i) PE: The Sb_2Te_3 outgrowths were removed and a planar surface was obtained by performing mechanical polishing and chemical etching of the substrate top surface after the MOCVD growth. In this process, the sample surface was grinded with a commercial Struers OP-U 0.04 µm colloidal silica suspension, followed by selective removal of the Sb_2Te_3 debris and residues by immersion in a 4.4 M HNO_3 solution for 5 s (selective etch of Sb_2Te_3) and then by immersion in a 1.25 M NaOH solution for 1 s (selective etch of the AAO template).

Postgrowth Processes ii) LP: A ≈500 nm thick Sb_2Te_3 film was formed on top of the NPs by prolonged MOCVD growth (240 min total growth time). A double-sided adhesive carbon strip was then glued to the Sb_2Te_3 film to fix the sample onto a copper plate. Finally, the Sb_2Te_3 NPs and film were liberated from the template by immersion in a 3.75 M NaOH solution for 10 min.

Characterization: The morphology of the NPs grown in the AAO templates was characterized by a Zeiss Supra 40 field emission SEM. An ItalStructures HRD3000 XRD instrument was used to evaluate the crystalline structure of the grown structures. The local microstructure and composition of the NPs were studied by a JEOL 2200FS TEM, with point resolution of 0.18 nm, equipped with an in-column Ω energy filter, 2 high-angle annular dark-field detectors, and EDX, on cross-section lamellae prepared by a Zeiss Auriga FIB out of the AAO templates after MOCVD growth. Raman characterization was performed in a z-backscattering geometry by using a Renishaw In-via Spectrometer, equipped with a 2.4 eV/514 nm continuous wave diode-pumped laser (RL 514C class 3B). The laser beam with an excitation wavelength of 514 nm was focused onto the sample by a 50 × Leica objective and 0.75 numerical aperture. The beam power at the sample was maintained in the range of (1–10) mW, in order to avoid laser-induced heating on the surface and sample damage. c-AFM was performed with a Bruker atomic force microscope (Dimension Edge) equipped with a tunneling AFM electrometer (1 pA to 1 µA current range). The conductive measurements were carried out in contact mode using highly doped diamond-coated tips (conductive diamond coated tip-contact mode and reflex coating, Nanosensors) with a typical radius of curvature of the tip in the 100–200 nm range. A bias voltage (in the 2–3 V range) was applied to the substrate, while the tip was electrically grounded.

Supporting Information

Supporting Information is available from the Wiley Online Library or from the author.

Acknowledgements

1901743 (7 of 9)

Conflict of Interest

The authors declare no conflict of interest.

Keywords

[1] B. Liu, Z. Song, S. Feng, B. Chen, *Microelectron. Eng.* **2005**, *82*, 168.

[2] G. W. Burr, M. J. Breitwisch, M. Franceschini, D. Garetto, K. Gopalakrishnan, B. Jackson, B. Kurdi, C. Lam, L. A. Lastras, A. Padilla, B. Rajendran, S. Raoux, R. S. Shenoy, *J. Vac. Sci. Technol., B: Nanotechnol. Microelectron.: Mater., Process., Meas., Phenom.* **2010**, *28*, 223.

[3] S. Twaha, J. Zhu, Y. Yan, B. Li, *Renewable Sustainable Energy Rev.* **2016**, *65*, 698.

[4] S. Morikawa, T. Inamoto, M. Takashiri, *Nanotechnology* **2018**, *29*, 075701.

[5] Y. M. Zuev, J. S. Lee, C. Galloy, H. Park, P. Kim, *Nano Lett.* **2010**, *10*, 3037.

[6] D. Hsieh, Y. Xia, D. Qian, L. Wray, F. Meier, J. H. Dil, J. Osterwalder, L. Patthey, A. V. Fedorov, H. Lin, A. Bansil, D. Grauer, Y. S. Hor, R. J. Cava, M. Z. Hasan, *Phys. Rev. Lett.* **2009**, *103*, 146401.

[7] Y. Takagaki, A. Giussani, J. Tominaga, U. Jahn, R. Calarco, *J. Phys.: Condens. Matter* **2013**, *25*, 345801.

[8] M. Boniardi, A. Redaelli, C. Cupeta, F. Pellizzer, L. Crespi, G. D'Arrigo, A. L. Lacaita, G. Servalli, in *2014 IEEE Int. Electron Devices Meet.*, IEEE, San Francisco, CA, USA **2014**, p. 29.1.1–29.1.4.

[9] S.-H. Lee, Y. Jung, H.-S. Chung, A. T. Jennings, R. Agarwal, *Phys. E* **2008**, *40*, 2474.

[10] S. Selmo, R. Cecchini, S. Cecchi, C. Wiemer, M. Fanciulli, E. Rotunno, L. Lazzarini, M. Rigato, D. Pogany, A. Lugstein, M. Longo, *Appl. Phys. Lett.* **2016**, *109*, 213103.

[11] R. Cecchini, S. Selmo, C. Wiemer, M. Fanciulli, E. Rotunno, L. Lazzarini, M. Rigato, D. Pogany, A. Lugstein, M. Longo, *Micro Nano Eng.* **2019**, *2*, 117.

[12] M. Tan, X. Wang, Y. Deng, Y. Hao, *Thin Solid Films* **2017**, *623*, 116.

[13] S. Yazji, E. A. Hoffman, D. Ercolani, F. Rossella, A. Pitanti, A. Cavalli, S. Roddaro, G. Abstreiter, L. Sorba, I. Zardo, *Nano Res.* **2015**, *8*, 4048.

[14] G.-H. Dong, Y.-J. Zhu, G.-F. Cheng, Y.-J. Ruan, *J. Alloys Compd.* **2013**, *550*, 164.

[15] B. Hamdou, J. Gooth, A. Dorn, E. Pippel, K. Nielsch, *Appl. Phys. Lett.* **2013**, *102*, 223110.

[16] S. S. Hong, Y. Zhang, J. J. Cha, X.-L. Qi, Y. Cui, *Nano Lett.* **2014**, *14*, 2815.

[17] J. Shen, J. J. Cha, *Nanoscale* **2014**, *6*, 14133.

[18] T. Eom, S. Choi, B. J. Choi, M. H. Lee, T. Gwon, S. H. Rha, W. Lee, M.-S. Kim, M. Xiao, I. Buchanan, D.-Y. Cho, C. S. Hwang, *Chem. Mater.* **2012**, *24*, 2099.

[19] B. Cheong, S. Lee, J. Jeong, S. Park, S. Han, Z. Wu, D.-H. Ahn, *Phys. Status Solidi B* **2012**, *249*, 1985.

[20] T. Eom, T. Gwon, S. Yoo, B. J. Choi, M.-S. Kim, I. Buchanan, S. Ivanov, M. Xiao, C. S. Hwang, *Chem. Mater.* **2015**, *27*, 3707.

[21] S.-H. Lee, Y. Jung, R. Agarwal, *Nat. Nanotechnol.* **2007**, *2*, 626.

[22] M. Longo, R. Fallica, C. Wiemer, O. Salicio, M. Fanciulli, E. Rotunno, L. Lazzarini, *Nano Lett.* **2012**, *12*, 1509.

[23] S. Selmo, S. Cecchi, R. Cecchini, C. Wiemer, M. Fanciulli, E. Rotunno, L. Lazzarini, M. Longo, *Phys. Status Solidi A* **2016**, *213*, 335.

[24] J.-K. Ahn, K.-W. Park, H.-J. Jung, S.-G. Yoon, *Nano Lett.* **2010**, *10*, 472.

[25] Z. Ma, S. Chai, Q. Feng, L. Li, X. Li, L. Huang, D. Liu, J. Sun, R. Jiang, T. Zhai, H. Xu, *Small* **2019**, *15*, 1805307.

[26] R. Huang, S. L. Benjamin, C. Gurnani, Y. Wang, A. L. Hector, W. Levason, G. Reid, C. H. De Groot, *Sci. Rep.* **2016**, *6*, 27593.

[27] S. L. Benjamin, C. H. (Kees) de Groot, C. Gurnani, A. L. Hector, R. Huang, E. Koukharenko, W. Levason, G. Reid, *J. Mater. Chem. A* **2014**, *2*, 4865.

[28] C. H. (Kees) de Groot, C. Gurnani, A. L. Hector, R. Huang, M. Jura, W. Levason, G. Reid, *Chem. Mater.* **2012**, *24*, 4442.

[29] H. Li, J. Cao, W. Zheng, Y. Chen, D. Wu, W. Dang, K. Wang, H. Peng, Z. Liu, *J. Am. Chem. Soc.* **2012**, *134*, 6132.

[30] S. L. Benjamin, C. H. de Groot, A. L. Hector, R. Huang, E. Koukharenko, W. Levason, G. Reid, *J. Mater. Chem. C* **2015**, *3*, 423.

[31] S. Gazibegovic, G. Badawy, T. L. J. Buckers, P. Leubner, J. Shen, F. K. de Vries, S. Koelling, L. P. Kouwenhoven, M. A. Verheijen, E. P. A. M. Bakkers, *Adv. Mater.* **2019**, *31*, 1808181.

[32] J. H. Jeong, S. J. Park, S. Bin An, D. J. Choi, *J. Cryst. Growth* **2015**, *410*, 47.

[33] C. A. Ihalawela, R. E. Cook, X. M. Lin, H. H. Wang, G. Chen, *MRS Proc.* **2012**, *1431*, mrss12.

[34] M. S. Sander, R. Gronsky, T. Sands, A. M. Stacy, *Chem. Mater.* **2003**, *15*, 335.

[35] S. Kim, Y.-I. Lee, Y.-M. Choi, H.-R. Lim, J.-H. Lim, N. V. Myung, Y.-H. Choa, *Nanotechnology* **2015**, *26*, 145503.

[36] C. Jin, G. Zhang, T. Qian, X. Li, Z. Yao, *J. Phys. Chem. B* **2005**, *109*, 1430.

[37] M. Longo, in *Advances in Non-Volatile Memory and Storage Technology* (Ed: Y. Nishi), Woodhead Publishing, Cambridge, England **2014**, Chs. 6, 7.

[38] W. Lee, S.-J. Park, *Chem. Rev.* **2014**, *114*, 7487.

[39] Z. Fan, H. Razavi, J. Do, A. Moriwaki, O. Ergen, Y.-L. Chueh, P. W. Leu, J. C. Ho, T. Takahashi, L. A. Reichertz, S. Neale, K. Yu, M. Wu, J. W. Ager, A. Javey, *Nat. Mater.* **2009**, *8*, 648.

[40] X. Wang, X. Sun, M. Fairchild, S. D. Hersee, *Appl. Phys. Lett.* **2006**, *89*, 233115.

[41] J. Zhang, L. Jin, S. Li, J. Xie, F. Yang, J. Duan, T.-H. Shen, H. Wang, *J. Mater. Sci. Technol.* **2015**, *31*, 634.

[42] E. Rotunno, L. Lazzarini, M. Longo, V. Grillo, *Nanoscale* **2013**, *5*, 1557.

[43] T. L. Anderson, H. B. Krause, *Acta Crystallogr., Sect. B: Struct. Crystallogr. Cryst. Chem.* **1974**, *30*, 1307.

[44] G. H. Han, D. L. Duong, D. H. Keum, S. J. Yun, Y. H. Lee, *Chem. Rev.* **2018**, *118*, 6297.

[45] X. Zhang, Z. Zeng, C. Shen, Z. Zhang, Z. Wang, C. Lin, Z. Hu, *J. Appl. Phys.* **2014**, *115*, 024307.

[46] M. Tan, Y. Deng, Y. Wang, B. Luo, L. Liang, L. Cao, *J. Electron. Mater.* **2012**, *41*, 3031.

[47] W. Liu, X. Peng, C. Tang, L. Sun, K. Zhang, J. Zhong, *Phys. Rev. B* **2011**, *84*, 245105.

[48] V. Bragaglia, F. Arciprete, W. Zhang, A. M. Mio, E. Zallo, K. Perumal, A. Giussani, S. Cecchi, J. E. Boschker, H. Riechert, S. Privitera, E. Rimini, R. Mazzarello, R. Calarco, *Sci. Rep.* **2016**, *6*, 23843.

[49] Inorganic crystal structure database (ICSD); Fachinformations-zentrum, **2017**, file no. 2084 for Sb$_2$Te$_3$, www2.fiz-karlsruhe.de/icsd_web.html.

ADVANCED
SCIENCE NEWS

www.advancedsciencenews.com

NANO · MICRO

small

www.small-journal.com

[50] G. Hao, X. Qi, Y. Fan, L. Xue, X. Peng, X. Wei, J. Zhong, *Appl. Phys. Lett.* **2013**, *102*, 013105.

[51] K. A. Kokh, V. V. Atuchin, T. A. Gavrilova, N. V. Kuratieva, N. V. Pervukhina, N. V. Surovtsev, *Solid State Commun.* **2014**, *177*, 16.

[52] K. M. F. Shahil, M. Z. Hossain, V. Goyal, A. A. Balandin, *J. Appl. Phys.* **2012**, *111*, 054305.

[53] W. Wu, G. Qiu, Y. Wang, R. Wang, P. Ye, *Chem. Soc. Rev.* **2018**, *47*, 7203.

[54] L. M. Goncalves, P. Alpuim, A. G. Rolo, J. H. Correia, *Thin Solid Films* **2011**, *519*, 4152.

[55] S. M. Souza, D. M. Trichês, J. C. de Lima, T. A. Grandi, R. S. de Biasi, *Phys. B* **2010**, *405*, 2807.

[56] S. A. Fortuna, X. Li, *Semicond. Sci. Technol.* **2010**, *25*, 024005.

[57] E. Rotunno, M. Longo, C. Wiemer, R. Fallica, D. Campi, M. Bernasconi, A. R. Lupini, S. J. Pennycook, L. Lazzarini, *Chem. Mater.* **2015**, *27*, 4368.

[58] C. Y. Kuo, C. Gau, *Thin Solid Films* **2011**, *519*, 3603.

[59] T. Shimizu, T. Xie, J. Nishikawa, S. Shingubara, S. Senz, U. Gösele, *Adv. Mater.* **2007**, *19*, 917.

[60] H. S. Shin, B. Hamdou, H. Reith, H. Osterhage, J. Gooth, C. Damm, B. Rellinghaus, E. Pippel, K. Nielsch, *Nanoscale* **2016**, *8*, 13552.

[61] M. J. Hampden-Smith, T. T. Kodas, *Chem. Vap. Deposition* **1995**, *1*, 39.

[62] B. J. Choi, S. Choi, Y. C. Shin, K. M. Kim, C. S. Hwang, Y. J. Kim, Y. J. Son, S. K. Hong, *Chem. Mater.* **2007**, *19*, 4387.

[63] K. W. Kolasinski, *Curr. Opin. Solid State Mater. Sci.* **2006**, *10*, 182.

[64] A. Giani, A. Boulouz, F. Pascal-Delannoy, A. Foucaran, A. Boyer, B. Aboulfarah, A. Mzerd, *J. Mater. Sci. Lett.* **1999**, *18*, 541.

[65] J. Kolar, J. M. Macak, K. Terabe, T. Wagner, *J. Mater. Chem. C* **2014**, *2*, 349.

[66] S. Shingubara, Y. Murakami, K. Morimoto, T. Takahagi, *Surf. Sci.* **2003**, *532–535*, 317.

[67] Y. Lei, W. Cai, G. Wilde, *Prog. Mater. Sci.* **2007**, *52*, 465.

[68] G. D. Sulka, in *Nanostructured Materials in Electrochemistry* (Ed: A. Eftekhari), Wiley-VCH Verlag GmbH & Co. KGaA, Weinheim, Germany **2008**, Ch. 1.

[69] D. Routkevitch, T. Bigioni, M. Moskovits, J. M. Xu, *J. Phys. Chem.* **1996**, *100*, 14037.

[70] H. Hardtdegen, M. Hollfelder, R. Meyer, R. Carius, H. Münder, S. Frohnhoff, D. Szynka, H. Lüth, *J. Cryst. Growth* **1992**, *124*, 420.

1901743 (9 of 9)